# Metasurface-enhanced mid-infrared spectrochemical imaging of tissues

S. Rosas[1], K. A. Schoeller [3,4], E. Chang[3,4], H. Mei[2], M.A. Kats[2], K.W. Eliceiri[1], X. Zhao[3,4], F. Yesilkoy[1,] *

[1]Department of Biomedical Engineering, University of Wisconsin-Madison, Madison, WI, USA

[2]Department of Electrical and Computer Engineering, University of Wisconsin-Madison, Madison, WI, USA

[3]Department of Neuroscience, University of Wisconsin-Madison, Madison, WI, USA

[4]Waisman Center, University of Wisconsin-Madison, Madison, WI, USA

*Corresponding author: filiz.yesilkoy@wisc.edu

## Supporting Information

## 1. Derivative spectroscopy

For quantitative and qualitative analysis in absorption spectrometry, a derivative of the measured spectra with respect to the wavenumber is often used. **Figure S1** shows the 1st – 4th order derivative spectra of a typical absorption band. For the second-order derivative of the absorption spectra, each absorption band maximum corresponds to a trough. In our quantitative analysis of specific bands, we calculated the area above the trough (see Figure S1) by using the trapezoidal rule. The area of the trough is expressed in a.u.[2]

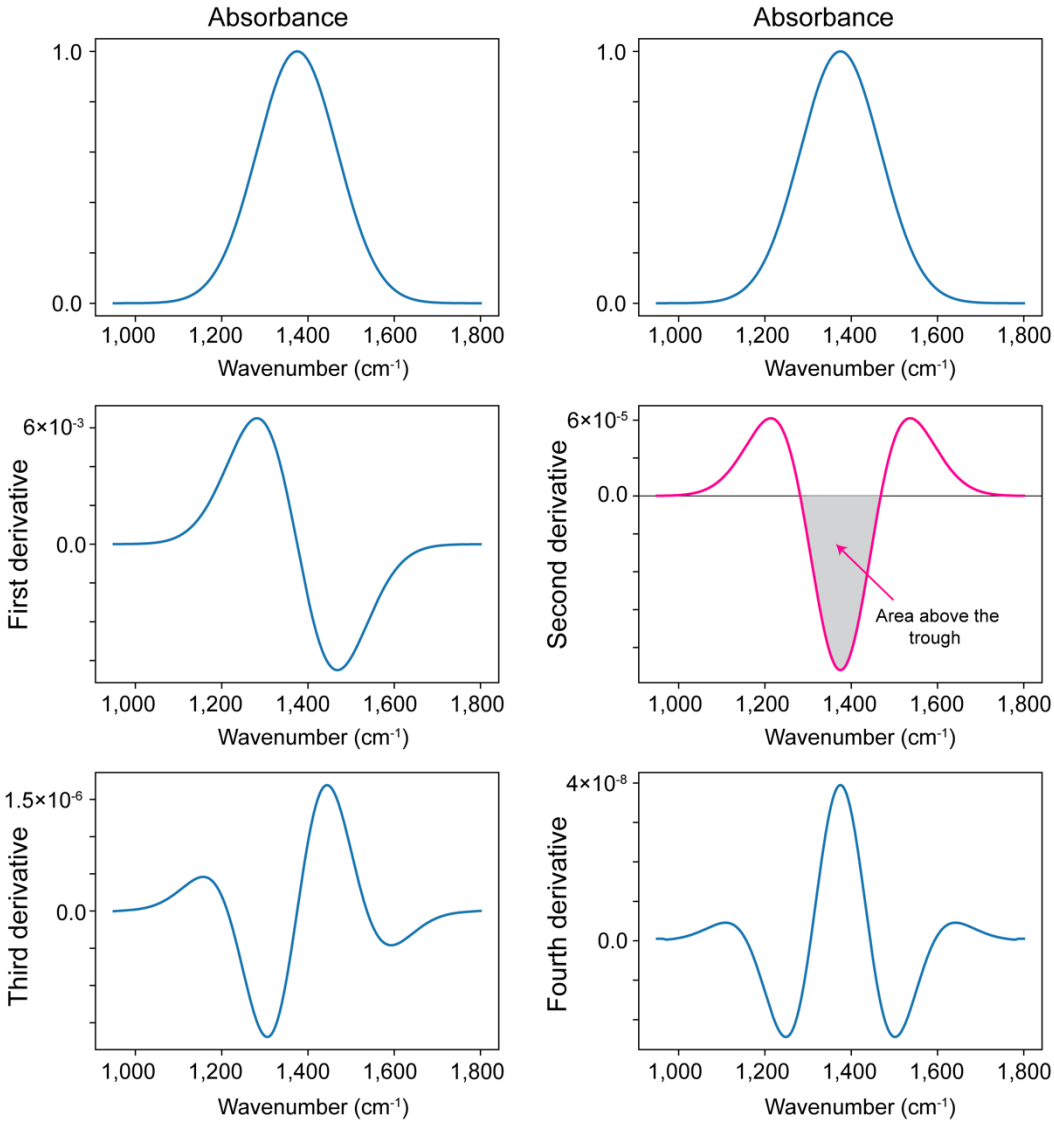


**Figure S1 | Absorbance and derivative spectra of a Gaussian band.** The absorbance signal was simulated using 512 data points and a standard deviation of 56. All derivatives were calculated using the Savitzky–Golay (SG) algorithm with a window length of 13 data points and a 2nd-order polynomial.

## 2. Plasmonic resonance mode analysis.

To interpret the physics of the plasmonic resonances supported by our metaunit design, which is composed of a complex cluster of nanostructures, we first use an intuitive mode hybridization model[1] and then support our findings with parameters extracted by the temporal coupled mode theory (TCMT)[2]. Our ulu-shaped composite plasmonic system supports three modes covering the fingerprint spectral range where we perform our measurements (5.5 – 10.5 μm). In the vertical (90°) polarization, we excite two spatially overlapping modes covering the low and high wavenumbers. Specifically, free-space propagating light effectively interacts with the center vertical rod, exciting its fundamental electrical dipolar resonance, which strongly interacts with the two u-shaped split ring resonators (SRR) on both sides of the rod. The strong coupling between the elementary radiative electric dipolar resonance of the center rod and the non-radiative fundamental magnetic modes of the side SRRs leads to a mode hybridization and results in spatially overlapping yet spectrally split plasmonic resonances[1] (**Figure S2**). In the horizontal (0°) polarization, the well-characterized radiative fundamental magnetic modes [3] of the SRRs are excited, which fills the spectral gap between the hybridized modes. Correspondingly, the hybridized modes excited by the vertical polarization can be tuned by changing the length of the center rod ($L_1$), where longer rod length leads to a redshift in both hybridized modes (**Figure S4a**). Moreover, the strong coupling-induced mode hybridization leading to the X-shaped anticrossing between the radiant dipolar resonance of the center rod and spectrally varying non-radiant magnetic SRR mode is shown in **Figure S4b**. In the horizontal polarization, the fundamental magnetic mode of the SRR can be tuned by changing vertical ($L_2$) and horizontal ($L_3$) lengths of the u-shape. Increasing $L_2$ and/or $L_3$ increases the total resonator length, therefore the magnetic resonance redshifts towards lower wavenumbers. The expected effects of the $L_2$ and $L_3$ parameters on the resonance position are in line with our simulation findings shown in Figure S4c and S4d.

**Temporal coupled mode theory – TCMT[2]:** The optical response of the ulu resonator can also be described by temporal coupled mode theory (TCMT). By utilizing a minimal set of fitting parameters (**Table S1**), TCMT accurately models the polarized reflectance spectra observed in both experimental data and finite-element simulations. Moreover, it provides a clear and comprehensive understanding of the ulu's resonance mechanism. TCMT describes the time-evolution of the resonator mode's amplitudes $\boldsymbol{a}$ by the following expressions:

$$\frac{d}{dt}\boldsymbol{a} = (j\boldsymbol{\Omega} - \boldsymbol{\Gamma})\boldsymbol{a} + \boldsymbol{K}^T\boldsymbol{s}_+ \tag{2}$$

$$\boldsymbol{s}_- = \boldsymbol{C}\boldsymbol{s}_+ + \boldsymbol{D}\boldsymbol{a} \tag{3}$$

where $|\boldsymbol{a}|^2$ represents the energy stored by a particular resonator, $|\boldsymbol{s}_+|^2$ is the incident power $|\boldsymbol{s}_+|^2 = c\,\epsilon_0/2\,\left|E_{x,y}\right|^2$, which is proportional the amplitude of the $x(or\ y)$ linearly polarized incident plane wave, and $\boldsymbol{s}_-$ corresponds to the scattered waves. Here, $\boldsymbol{\Omega}$ is a $N\times N$ matrix with mode resonance frequencies along its diagonal and near-field coupling rates off-diagonal

elements, $\boldsymbol{\Gamma}$ is determined by the mode radiative damping ($\gamma_1\ \gamma_2 \cdots \gamma_N$), and radiative coupling rates, $\boldsymbol{D}$ corresponds to coupling strength between the resonators, $\boldsymbol{C}$ is the direct port-port coupling and $\boldsymbol{I}$ is the identity matrix of size $N \times N$. These matrices are formally defined as:

$$\boldsymbol{\Gamma} = \left(\sqrt{\gamma_1}\sqrt{\gamma_2} \cdots \sqrt{\gamma_N}\right)^T \left(\sqrt{\gamma_1}\sqrt{\gamma_2} \cdots \sqrt{\gamma_N}\right)$$
$$\boldsymbol{K} = \boldsymbol{D} = (1\ 1)^T \left(\sqrt{\gamma_1}\sqrt{\gamma_2} \cdots \sqrt{\gamma_N}\right)$$
$$\boldsymbol{C} = \begin{pmatrix} 0 & -1 \\ -1 & 0 \end{pmatrix} \tag{4}$$

Solving Equation 2 for $\boldsymbol{a}$ and substituting its value in Equation 3 yields:

$$\boldsymbol{a} = (j\omega\boldsymbol{I} - j\boldsymbol{\Omega} + \boldsymbol{\Gamma})^{-1}\boldsymbol{K}^T\boldsymbol{s}_+ \tag{5}$$

$$\boldsymbol{s}_- = \begin{pmatrix} s_{11} & s_{12} \\ s_{21} & s_{22} \end{pmatrix}\boldsymbol{s}_+ = [\boldsymbol{C} + \boldsymbol{D}(j\omega\boldsymbol{I} - j\boldsymbol{\Omega} + \boldsymbol{\Gamma})^{-1}\boldsymbol{K}^T]\boldsymbol{s}_+ \tag{6}$$

Where $(s_{12},\ s_{21})$ and $(s_{11},\ s_{22})$ are the reflection and transmission coefficients, respectively. Resonance frequencies, near-field coupling rates, and damping coefficients were calculated by fitting a Lorentzian model to the experimental single-resonant reflectance spectra measurements (Table 1S). Comparison between resonance peak for 90° polarization and 0° polarization are shown in **Figure S3**. The TCMT remarkably captures the main spectral features of the polarization-multiplexed multi-resonance plasmonic metasurface.

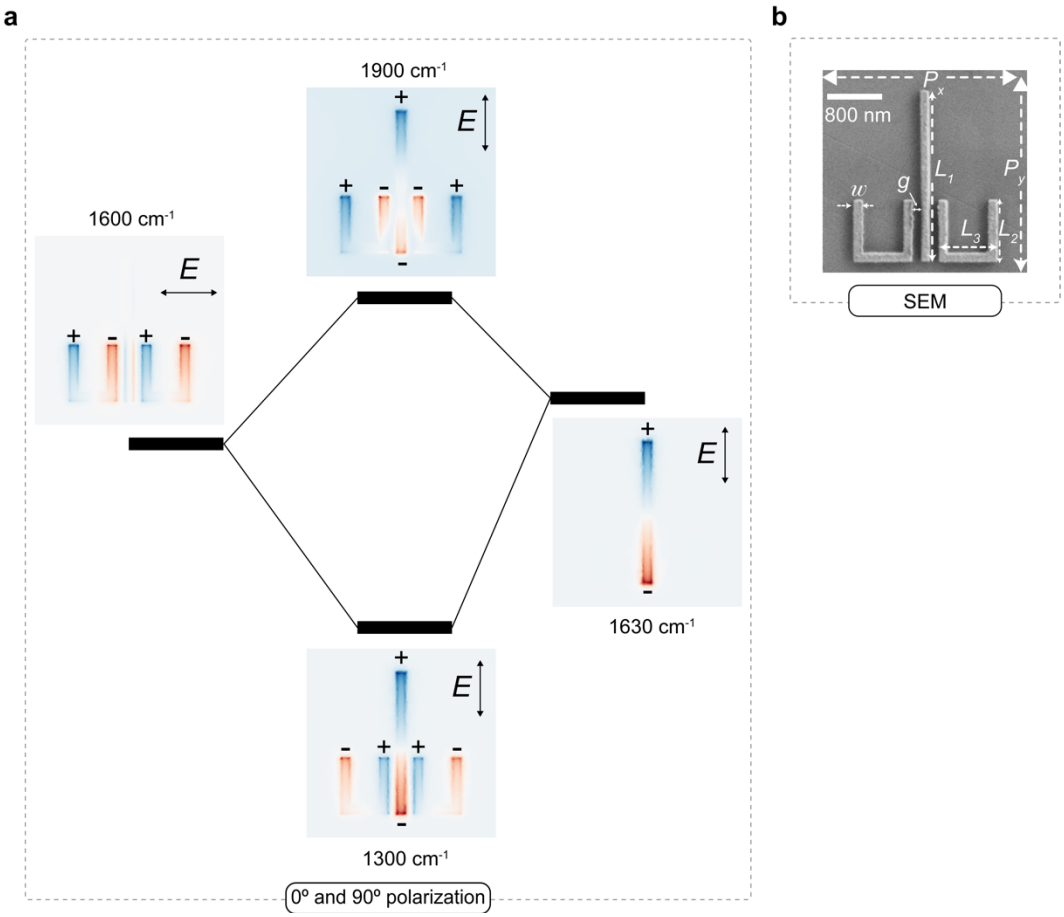

**Figure S2 | Schematic representation of the three different resonance modes of the ulu-shaped metaunit coupled to the incident mid-infrared light. a**, Mode hybridization scheme shows the strong coupling between the radiant center rod and non-radiant u-shaped split ring resonator leading to spectrally split, spatially overlapping resonances at the high (1900 $cm^{-1}$) and low (1300 $cm^{-1}$) wavenumbers. Fundamental magnetic mode of the u-shaped split ring resonator (1600 $cm^{-1}$) only becomes radiant with horizontal excitation. **b,** Fabricated metaunit geometry. All simulation results show the normalized electric field z-component maps at the resonance frequencies.

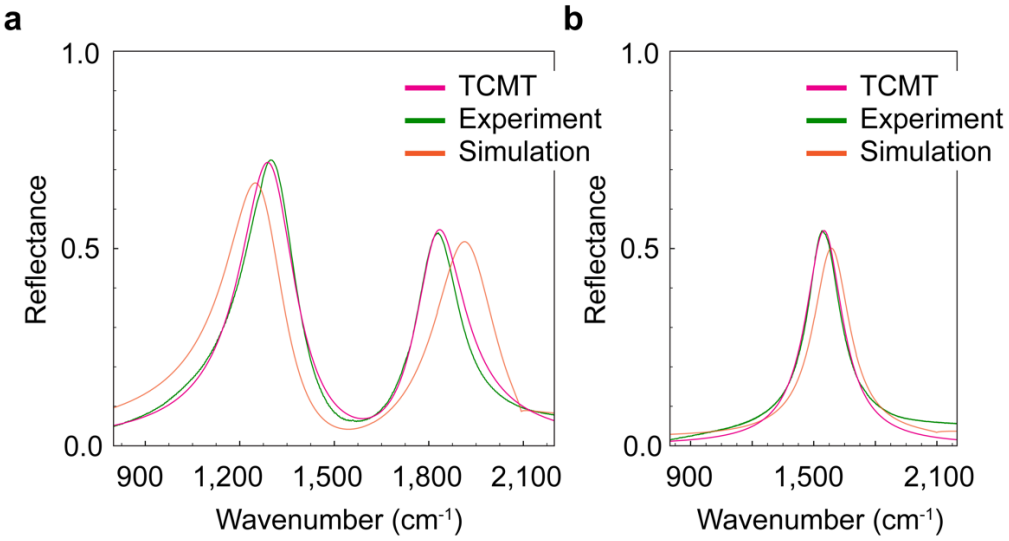


**Figure S3 | Temporal-coupled-mode theory modeling.** Experimental reflectance spectrum vs. calculated resonance modes derived by the TCMT model at **a**, 90° and **b**, 0° polarization.

**Table S1** | Mode resonance frequencies and damping rates.

| Polarization | Resonance frequency ($\boldsymbol{\Omega_{ij,i=j}}$) ($cm^{-1}$) | Radiative damping rate ($\gamma_N$) ($cm^{-1}$) | Near-field coupling($\boldsymbol{\Omega_{ij,i\neq j}}$) ($cm^{-1}$) |
|---|---|---|---|
| 90° polarization | 1300 + 30j | 105 | 120 |
| | 1900 + 45j | 25 | 120 |
| 0° polarization | 1600 + 50i | 60 | 0 |

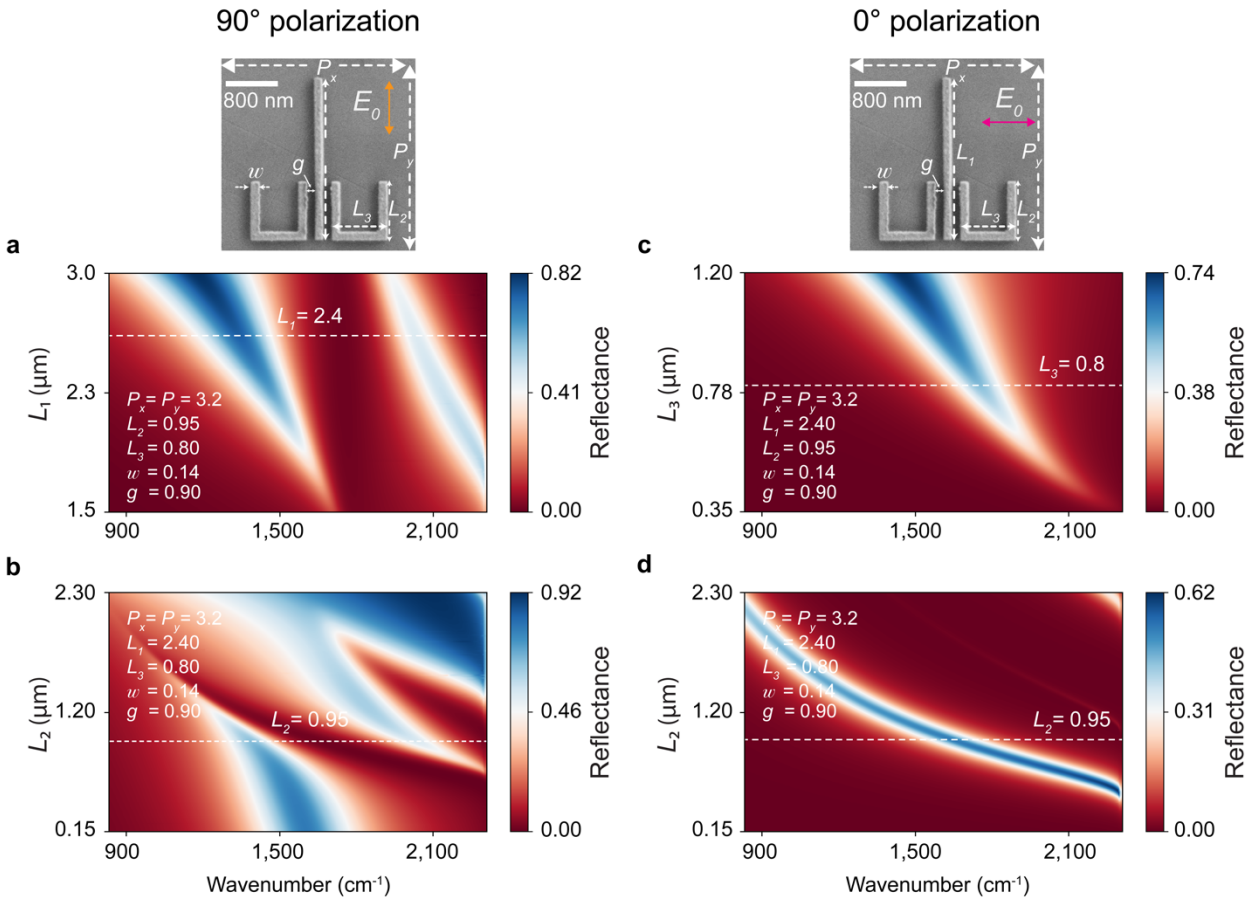


**Figure S4 | Simulation of the plasmonic resonance mode tunning by varying geometric *L₁*, *L₂*, and *L₃* parameters.** For both polarizations all parameters were fixed as $P_x$ = 3.2 µm, $P_y$ = 3.2 µm, $L_1$ = 2.40 µm, $L_2$ = 0.95 µm, $L_3$ = 0.8 µm, $g$ = 0.14 µm, and $w$ = 0.14 µm; 90 nm thick, with only one parameter swept at a time. At 90° polarization **a**, Parametric variation of $L_1$ from 1.5 µm to 3.0 µm. **b**, Parametric variation of $L_2$ from 0.15 µm to 2.30 µm are shown. At 0° polarization **c**, Parametric variation of $L_3$ from 0.35 µm to 1.20 µm, and **d**, Parametric variation of $L_2$ from 0.15 µm to 2.30 µm are shown. The parameters indicated by the white dashed lines were fabricated and used in the SE-MIRSI measurements. All units in (µm).

## 3. Plasmonic field enhancement and localization.

Plasmonic 'ulu' metasurface E-field intensity decay length into the top media at one of its resonance wavenumbers ($\upsilon = 1300$ cm$^{-1}$)

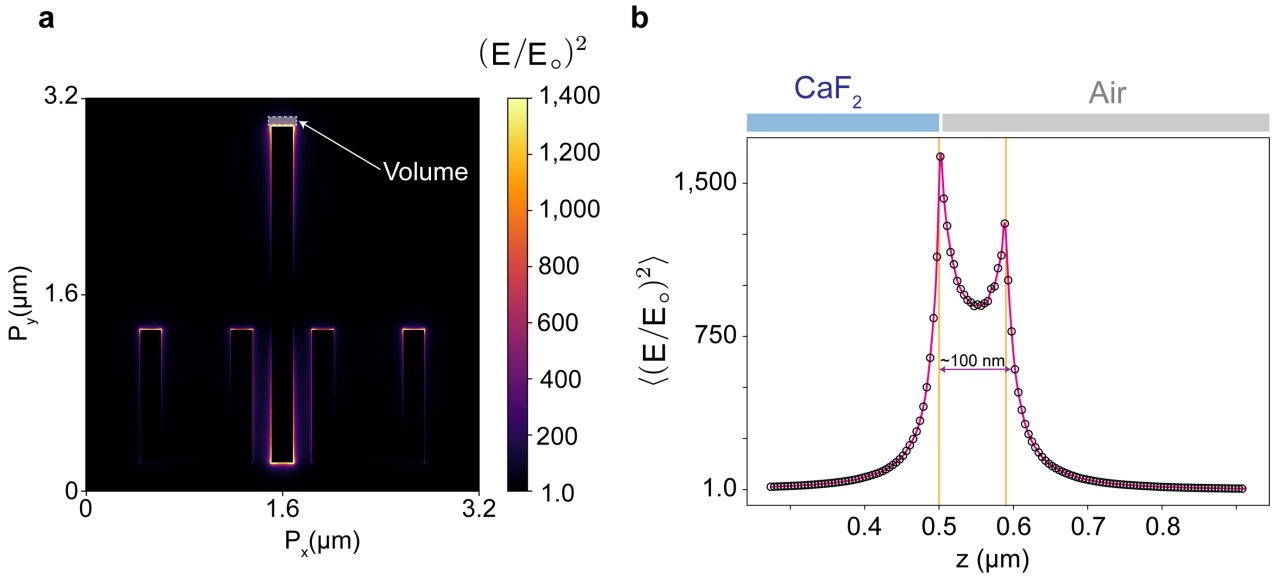


**Figure S5 | Plasmonic metasurface E-field decay length at its resonance wavenumber. a**, Near-field distribution at $z$ = 590 nm. Strong E-field enhancement is shown in bright yellow color for $\upsilon = 1300$ cm$^{-1}$. **b**, E-field intensity enhancement in the sampling volume shown in panel **a**, along the z-direction. Volume region extends out 20 nm from tip-face of the center rod.

## 4. Tissue adherence.

To ensure that our tissue transfer procedure yields a uniform contact between the tissue and the metasurface, we compared the spectra from the following two samples: 1) We first measured a freshly cut brain tissue section transferred onto the plasmonic metasurface as detailed in the methods section. 2) Next, we sandwiched the tissue between a microscope glass slide and the metasurface chip and used two binder clips as clamps to apply a pressure on the tissue. In **Figure S6**, we present spectra from a similar brain region measured with and without the applied pressure on the tissue. Our results show that there were no significant differences in the absorbance spectra implying that tissue was in contact with the substrate after transfer.

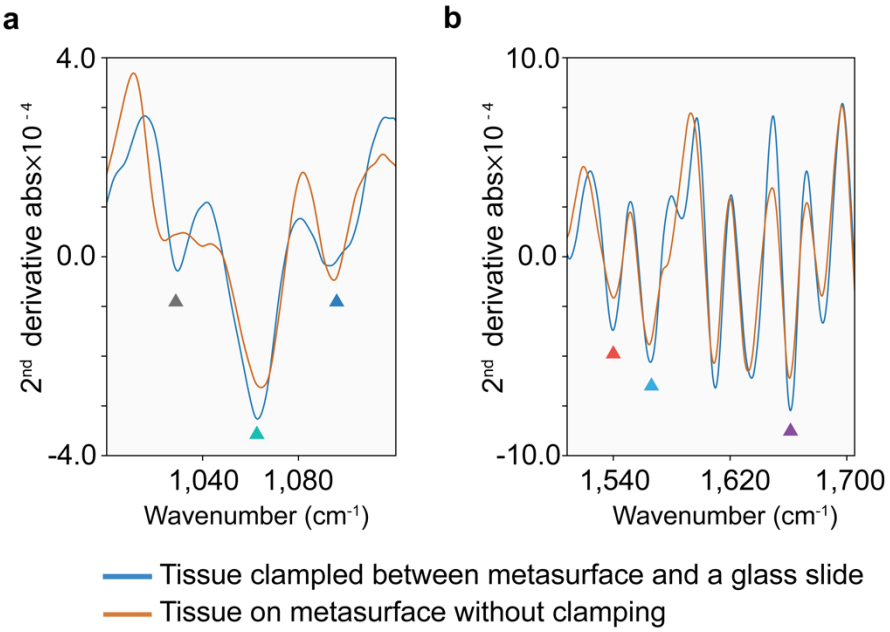


**Figure S6 | Tissue adherence**. 2nd derivative absorbance spectra for a 20-µm brain tissue section recorded from a similar region with and without clamping with a top glass slide. **a**, Molecular fingerprints of glycogen (1024 $cm^{-1}$ ▲), deoxyribose (1060 $cm^{-1}$ ▲), symmetric phosphate (1090 $cm^{-1}$ ▲). **b**, β-sheet (1542 $cm^{-1}$ ▲), amide II (1574 $cm^{-1}$ ▲), and amide I (1660 $cm^{-1}$ ▲).

## 5. Plasmonic ‘ulu’ Metasurface Fabrication steps.

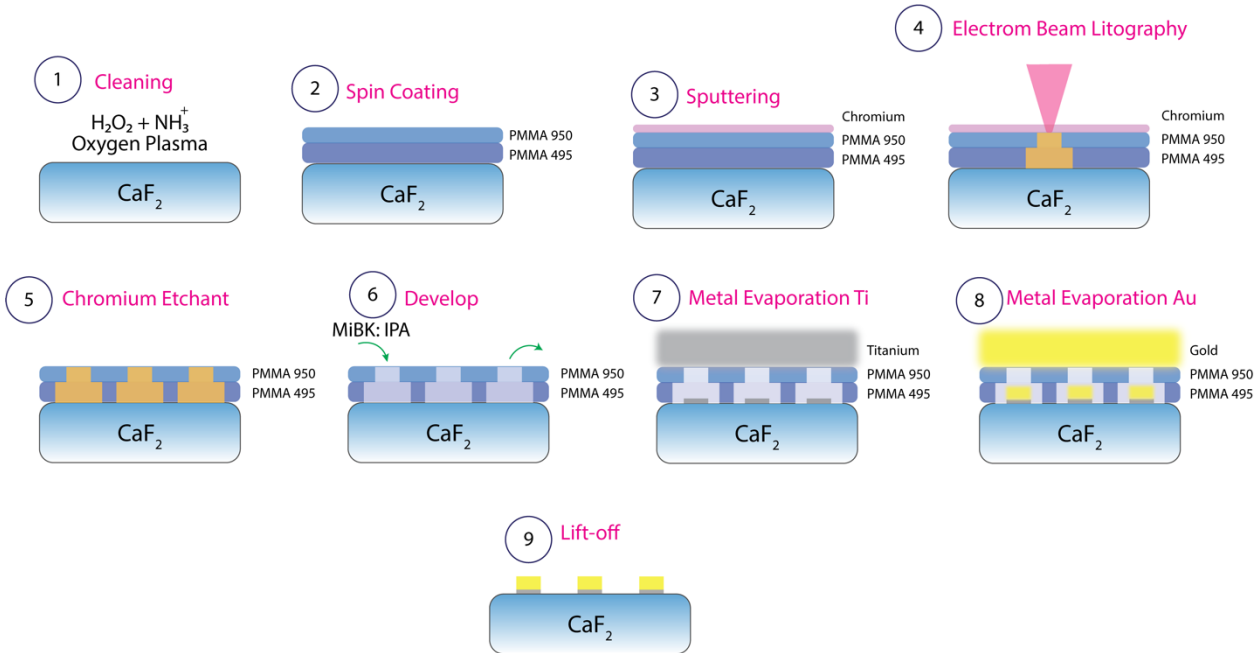


**Figure S7 | Cleanroom fabrication steps for ulu plasmonic metasurface.**

## 6. Data reproducibility and statistical test results

**Figure S8** displays the second derivative absorption spectra of three 20 µm brain tissue sections that were collected by SE-MIRSI using three different brand-new plasmonic metasurfaces. The plot shows the solid lines that represent the averages of the spectra, while the shaded regions indicate two standard deviations (mean ± std). The reference spectrum, represented by the dashed line, is obtained from a brain tissue section with a thickness of 20 µm that was mounted on a gold mirror and referenced to a front-surface gold mirror. For repeatability a total of 4096-pixel spectra were selected from each plasmonic metasurface to compare their performance in collecting absorption spectra of brain tissue sections. The shaded regions highlight the level of variation between the different spectra collected on each metasurface, providing a basis for comparison with the reference spectra for all three different samples.

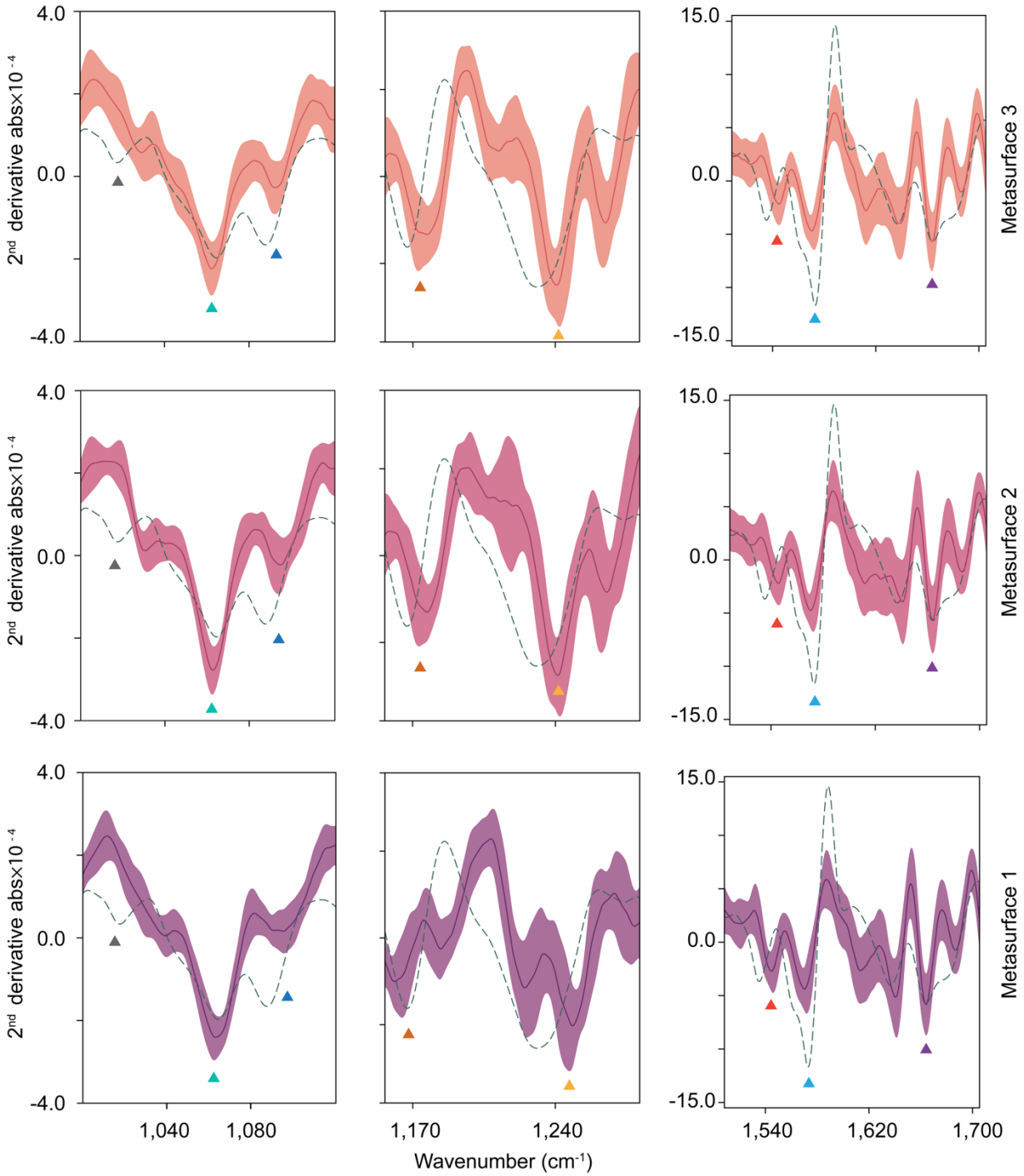


**Figure S8 | Second derivative absorption spectra of three 20 µm brain tissue sections collected by SE-MIRSI on three different brand-new plasmonic metasurfaces.** The solid lines are averages, and the shaded regions correspond to two standard deviations (mean ± std). Reference spectra (dashed lines) were measured from brain tissue section with thickness 20 µm, mounted on a gold mirror and was referenced to a clean gold mirror. A total of 4096-pixels spectra were considered from each metasurface.

We conducted a statistical analysis to demonstrate the effectiveness of our SE-MIRSI method in detecting and quantifying functional biomolecules from constant nanoscale tissue volumes compared to the conventional MIRSI. To accomplish this, we computed median absorbance values for 80 and 20 µm-thick tissue sections from the integral band distributions measured on the $CaF_2$ and the ulu-metasurfaces (data shown in **Figures 2** and **4**). Next, we calculated the ratio of the median absorbance values from 80 and 20 µm thick tissues for each band, which we call 80/20 ratio parameter. As expected in MIRSI measurements, for deoxyribose (1060 $cm^{-1}$ ▲), symmetric phosphate (1090 $cm^{-1}$ ▲), asymmetric phosphate (1236 $cm^{-1}$ ▲), and β-sheet (1542 $cm^{-1}$ ▲) bands, the 80/20 ratios are 4 times larger than the SE-MIRSI measurements using the ulu-metasurfaces. This is due to the optical path length dependency on absorption signals in MIRSI. For the protein range, Amide II (1574 $cm^{-1}$ ▲), and amide I (1660 $cm^{-1}$ ▲) the 80/20 ratio drops to 2.85 and 2.23, respectively, because of signal saturation of the strong amide bands in the 80 µm thick tissues. A two-tailed unpaired t-test was used to compare the 80/20 ratios between the brain tissue section on bare CaF2 and on the plasmonic metasurface. A p-value of $p = 5.74\times10^{-4}$ was identified between the 80/20 ratios for deoxyribose (1060 $cm^{-1}$ ▲), symmetric phosphate (1090 $cm^{-1}$ ▲), asymmetric phosphate (1236 $cm^{-1}$ ▲), and β-sheet (1542 $cm^{-1}$ ▲) bands (see **Figure S9**). In all cases, significance was defined as $p<0.05$.

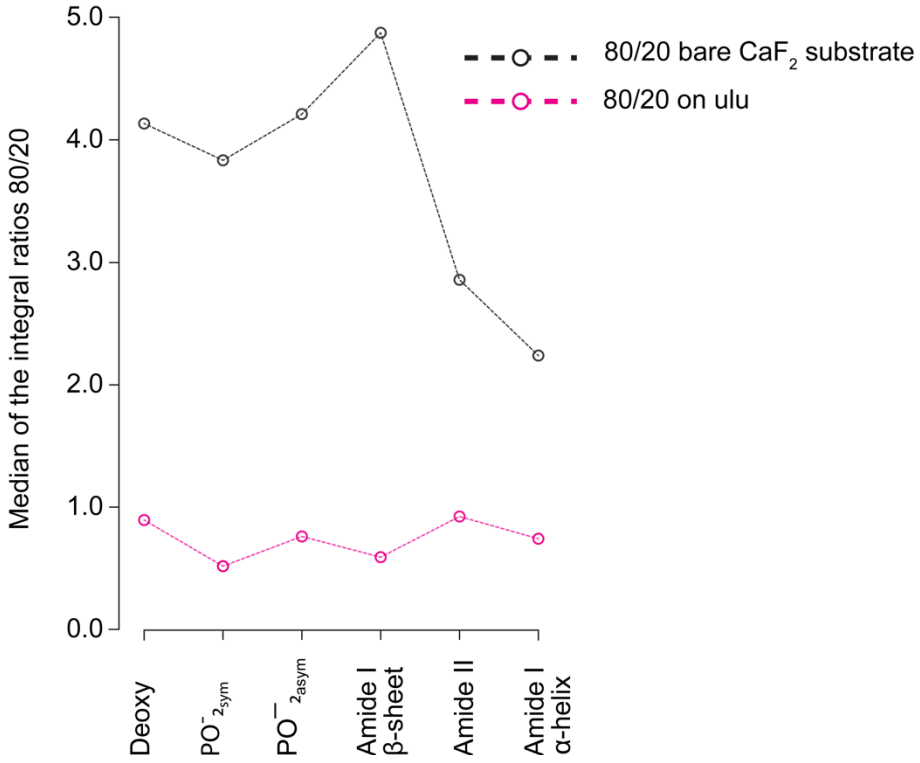


**Figure S9 | Tissue thickness effects on quantitative absorption band analysis in SE-MIRSI and MIRSI measurements.** Median band absorbance values for 80 and 20 µm thick-tissue sections were calculated from the integral distributions of brain tissue sections on the $CaF_2$ and the ulu-metasurface (**Figure 2** and **Figure 4**). Overall, median 80/20 ratio of the SE-MIRSI measurements

using the ulu-metasurfaces are steady across the entire band range showcasing the retrieval of molecular fingerprints of a heterogenous sample from constant nanoscale volumes.

## References


[1] E. Prodan, C. Radloff, N. J. Halas, P. Nordlander, *Science* **2003**, *302*, 419.
[2] H. A. Haus, *Waves and Fields in Optoelectronics*, Prentice Hall, Englewood Cliffs, NJ, **1984**.
[3] S. Linden, C. Enkrich, M. Wegener, J. Zhou, T. Koschny, C. M. Soukoulis, *Science* **2004**, *306*, 1351.